Acoustofluidic Three-Dimensional Motion of Suspended Cells at Near-Zero Acoustic Contrast in Homogeneous Media

Mahdi Rezayati Charan, Filip Berg, and Per Augustsson [*]

Department of Biomedical Engineering, Lund University, Ole Römers väg 3, 22363 Lund, Sweden

Acoustic separation of suspension cells can be achieved by altering the properties of the cell medium. Cells of different types can then migrate in opposing directions in the sound field due to differences in their relative density and compressibility with respect to the surrounding fluid. For near-zero acoustic contrast the acoustic radiation force on cells becomes negligible, and it is the primary objective of this paper to study the interplay of acoustic radiation, acoustic streaming, and buoyancy in this regime and how it may affect the separation outcome. We study the three-dimensional acoustophoretic motion of suspension cells in homogeneous suspending media and link this to the underlying acoustofluidic mechanisms. Cell trajectories are measured by a defocused-image tracking approach, and we assess the technique's applicability for tracking cells by determining the associated error when measuring the out-of-image-plane component of the tracks. For cells at near-zero acoustic contrast, we observe strong effects of buoyancy and acoustic streaming and that small distributions of cell properties within a population leads to large differences in the cell motion patterns. A neural network was developed to classify experimental cell trajectories according to their acoustic contrast in different suspending media. Further, we compare the experimentally measured trajectories to a numerical model by generating simulated trajectories of cells.

I. INTRODUCTION

Over the past decade, microfluidics has been identified as an enabling future technology for cell handling, separation, and analysis [1,2], facilitating cell-based assays in health care and biotechnology research to be carried out in a shorter time frame and with less consumption of reagents. At the same time, the accuracy of measurements on cells offered by microfluidics has the potential to rival the current gold standards [3]. Along with the microfluidic developments in spatial manipulation of micro-objects, single-cell phenotyping for investigating cell-intrinsic biomechanical properties has become an emerging field [4]. Label-free approaches based on cells' biophysical properties are then utilized to distinguish different cell types from one another by their migration relative to an applied field. Biophysical signatures such as size [5–7], density [8–10], deformability [11–13], electrical [14], magnetic [15,16], and optical [17,18] properties have been studied to gain insights into cells' biophysical fingerprints in different conditions. Since, in most of

these methods, the same applied field can be employed to both analyze and separate cells, accurate measurements of single-cell properties can be directly utilized to improve the separation performance of cells [14].

The present work deals with acoustophoresis, an approach for positioning, separating, and mechanophenotyping cells. Acoustophoresis offers a gentle and noninvasive tool for handling cells and has been reported not to cause alterations in cell viability, proliferation, DNA damage, or function [19,20]. Acoustic waves generate forces on suspension cells by sound scattering in a microfluidic chamber. The cell migration in the field is governed by the cell size and differences in mass density, and compressibility of the cell relative to the surrounding medium [21,22]. Typically, the separation of cells in acoustophoresis is based on larger cells experiencing stronger forces than small cells, and the cells are therefore pushed sideways by an acoustic field that is oriented orthogonally to a flow [23–26]. Such a scheme has been employed to concentrate cells [27,28], generate plasma for whole blood [29], or to transfer cells or functionalized capture beads between two media [30].

The ability to discriminate cells of different type by means of an acoustic field can be dramatically improved by selecting a suspending medium that causes the cells to move in opposite directions due to differences in their acoustic properties. But for cells that have similar or partly overlapping density or compressibility, the acoustic

---

[*]per.augustsson@bme.lth.se

contrast is inevitably low for any such media, leading to relatively low acoustic radiation forces acting on the cells. This means that other transport phenomena can instead dominate the migration of cells. This work aims to investigate cell motion in response to sound in homogeneous suspending media in a bulk acoustic half standing wave inside a rectangular cross section resonator and link this to underlying acoustofluidic mechanisms. Our primary focus has been to understand the influence of acoustic streaming and buoyancy for biological cells with near-zero acoustic contrast. The acoustic radiation force changes sign based on the acoustic contrast, which depends on the relative density and compressibility of the suspended cells with respect to the surrounding fluid. Positive acoustic contrast leads, in this configuration, to cells being pushed towards the center of the channel, whereas negative acoustic contrast causes cells to migrate towards the walls. When the magnitude of the acoustic contrast factor is close to zero, the radiation force is negligible, and cells follow the slow but steady acoustic streaming rolls that were described analytically by Lord Rayleigh [31]. Previous work on suspended microspheres has shown that they follow complex three-dimensional (3D) trajectories due to a combination of primary radiation forces, acoustic streaming flow, and gravity [32,33]. The resulting trajectory is thus highly dependent on the size, density, and compressibility of the suspended particle as well as the density, compressibility, and viscosity of the suspending medium. Microparticles are, however, far from optimal models for cells in the context of acoustofluidics since they are highly spherical, and uniform in size and material properties. Importantly, the compressibility of off-the-shelf microparticles, based on polystyrene (PS), melamine, and polymethyl methacrylate, deviates from that of cells, and water-based fluids, by a factor of 2 or more [34]. To achieve negative contrast for microparticles, solute molecules must be added to the medium in amounts that result in either high viscosity, which increases the drag forces slowing particles down, or high density, which makes the particles highly buoyant. Taken together, phenomena related to zero or negative acoustic contrast of cells are best studied directly on cells.

Direct measurements of cells' responses to sound in standard cell media have previously been carried out by mapping the positions of cells in the x-y plane [35–40]. By studying the 2D motion, and final location of cells in an acoustic field for increasing concentrations of the solute molecule iodixanol, Dabbi *et al.* [41] reported differences between activated and nonactivated T-cells, and Olofsson *et al.* [42] investigated viable and dead cells for three different cell types. Beyond a threshold concentration of iodixanol, viable cells were driven to the pressure antinode, while the dead cells were always retained in the pressure node due to being permeable to the surrounding medium. A previous study has shown that blood cells can be continuously acoustically fractionated in a density-modified medium based on differences in their effective acoustic impedances [43]. But to date, the effects of buoyancy and acoustic streaming near zero acoustic have not been systematically charted. Moreover, acoustic streaming and radiation can be difficult to resolve purely based on 2D measurements since both have a sinusoidal dependency on the standing acoustic wave when viewed along the z axis.

The z-component of a 3D behavior has recently been measured for bacteria on a standard phase-contrast microscope. Three-dimensional bacterial tracking was carried out by image cross-correlations between the observed diffraction patterns and a reference library. The technique is simple and easy to use but limited to a micron-scale resolution over $350 \times 300 \times 200$ µm. Going beyond such a volume to investigate bacterial motility was reported to constrain the performance [44].

This study investigates the 3D motion of suspended cells due to acoustic radiation and acoustic streaming inside an acoustofluidic resonator by general defocusing particle tracking (GDPT) [45,46]. We show that the GDPT method can be used to track fluorescently labeled suspension cells in three dimensions. We then investigate the response to sound of three types of cells in media of increasing acoustic impedance and classify their trajectories into three categories. For cells near zero acoustic contrast, we observe the effects of buoyancy and acoustic streaming, and how variation in cell properties within a population leads to different cell motion patterns. Further, we compare the experimentally measured trajectories to theory by generating trajectories of cells by numerical modeling.

II. MATERIALS AND METHODS

A. Cell culture and staining

We analyzed human neutrophils and the cell lines Jurkat (Clone E6-1, Sigma-Aldrich) and K562 leukemia (from Pereira lab, Division of Molecular Medicine and Gene Therapy, Lund University). Neutrophils were isolated directly from blood samples using an EasySep™ direct human neutrophil isolation kit (Stemcell Technologies, Norway). Blood was collected from healthy volunteers. The procedure includes written informed consent, following the Helsinki Declaration, and was approved by the Swedish ethical review authority (ref. no. 2020-05818). Collected neutrophils were washed and resuspended in phosphate-buffered saline (PBS, Sigma-Aldrich). Jurkat and K562 cells were cultured in T75 flasks and suspended in the recommended cell medium consisting of RPMI-1640 (Sigma-Aldrich) supplemented with 10% fetal bovine serum (FBS, Sigma-Aldrich) and 1% penicillin-streptomycin (Sigma-Aldrich). Cells were cultured at 37 °C under a 5% CO_2 atmosphere and passaged by splitting every 2–3 days.

Two types of fluorescence dyes were used to stain cells for microscopy imaging; cell-permeant CellTrace™ calcein red-orange, AM (ThermoFisher), and Calcein Deep Red™ AM ester (AAT Bioquest). First, the required number of cells suspended in the culture medium was collected in a tube and centrifuged before staining. Then the supernatant was discarded, and the cells were incubated at 37 °C for 20 min in PBS with 1 μM of fluorescence dye. Finally, after two centrifugation steps, the cells were resuspended in PBS with 2% FBS at a concentration of 2×10^6 cells per milliliter.

B. Density media preparation

We used Optiprep™ (Stemcell Technologies, Norway) containing 60% w/v iodixanol as an agent to prepare solutions with varying density and compressibility by adjusting the iodixanol concentrations in the range from 10% to 34%. Stained cells suspended in PBS with 2% FBS were stored on ice before the experiments. Density-adjusted solutions were prepared by adding a required amount of the Optiprep™ to the cell suspension.

C. Experimental set-up and procedure

An acoustofluidic glass-silicon-glass chip of length 70 mm and width 4 mm was fabricated (GeSim Bioinstruments and Microfluidics mbH, Germany) by etching a channel of length 50 mm and width $W = 375$ μm through an $H = 150$ μm thick silicon wafer by deep reactive ion etching, which was anodically bonded between two glass lids of thickness 500 and 610 μm, respectively [Figs. 1(a) and 1(b)], with sandblasted holes through the thinner side. A piezoceramic transducer (Pz26, Ferroperm™ piezoceramics, Meggit A/S, Denmark) resonant at 2 MHz (Supplemental Material, Fig. S1 [47]) and $30 \times 4.0 \times 1.0$ mm in size was bonded underneath the chip using cyanoacrylate glue (Loctite Super Glue, Henkel Norden AB, Stockholm,
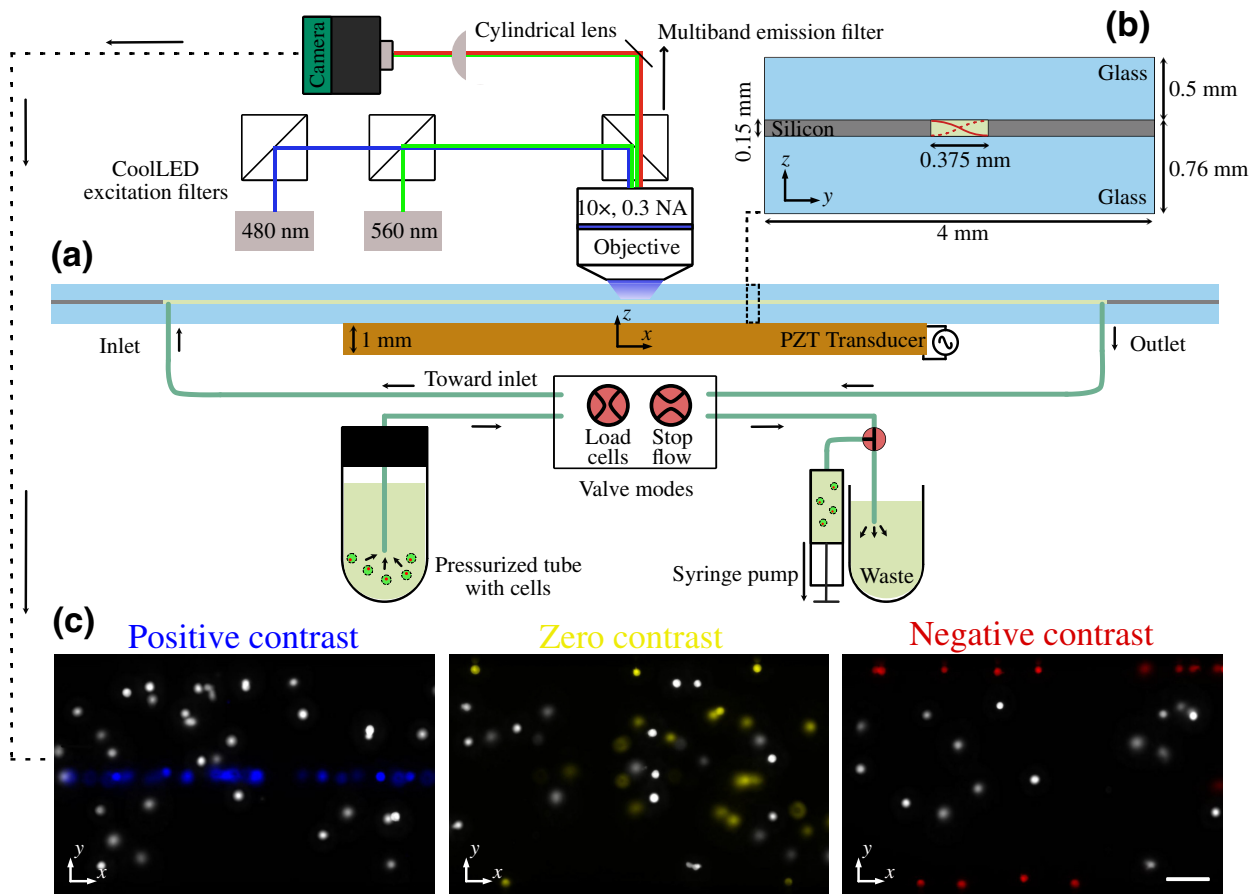

FIG. 1.   Schematic illustration of the experimental setup. (a) A cross-section view from the side (z-x) of the glass-silicon-glass chip mounted under the microscope, including the optical configuration, is shown. The optical path includes a replaceable cylindrical lens for imaging. A syringe pump is placed at the outlet to withdraw the suspending medium from a pressurized inlet reservoir, and a second reservoir beside the syringe pump collects the waste when emptying the syringe. To stop the flow, the valve switches to the stop-flow mode. (b) The radial cross-section (z-y) of the microchannel with all the dimensions. (c) The camera view of K562 cells in three different regimes of acoustic contrast as composite images of the first and last frame of a sequence of acquired images. The initial location of the cells is shown in gray scale and the final position after sound actuation with three different colors corresponding to positive (blue), zero (yellow), and negative (red) acoustic contrast. The scale bar is 75 μm.

Sweden). The transducer was driven by a function generator (AFG3022B, Tektronix, Inc., Beaverton, OR, USA) to deliver a frequency sweep (1.8–2.1 MHz), with 1 ms sweep time and 9 $V_{p.p.}$ as measured over the piezo with an oscilloscope (TDS1002, Tektronix, Inc., Beaverton, OR, USA). A Pt100 thermo-resistive element was glued to the piezoelectric transducer to record the temperature.

An epifluorescence microscope (BX51WI, Olympus Corporation, Tokyo, Japan), with a $10\times$, 0.3 numerical aperture (NA) objective, equipped with a CMOS camera (ORCA- Flash 4.0 V3, Hamamatsu Photonics KK, Japan) was used for imaging. To enhance the measurement depth, elliptically shaped defocused cell images were obtained by inserting a cylindrical lens with a focal length of 300 mm between the camera and the objective at a distance of 20 mm from the camera sensor [Fig. 1(a)]. A triple-wavelength LED unit (CoolLED pE-300^{ultra}, UK) supplied the illumination for fluorescence imaging of the PS particles and cells. We used fluorescent green (PS) beads with nominal diameters of 1.1 and 4.9 μm (Molecular Probes, Thermo Fisher Scientific, Waltham, MA) to calibrate the acoustic field before or after the cell experiments.

The excitation channels of the LED unit, activated through triggering from multiple transistor-transistor logic inputs, were equipped with single-band excitation filters (ET395/25x, ET480/30x, and ET560/25x Chroma Technology Corp, USA). A multiband emission filter (69013 bs, Chroma Technology Corp, USA) with the corresponding dichroic mirror (69013 m, Chroma Technology Corp, USA) was mounted in the microscope filter turret to facilitate fast sequential multichannel acquisition.

The timed acquisition was controlled via trigger signals from an Analog Discovery 2 data acquisition system (Digilent, USA). The synchronized signals were used to trigger the CMOS camera and different LED unit excitation channels for imaging purposes.

The flow in the system was controlled through a pressurized tube holder (Elveflow adaptor for Falcon© tubes) at the channel inlet and a syringe pump (Tricontinent C-series, Gardner Denver, USA) equipped with a rotary three-port T-valve located at the channel outlet to facilitate priming of the system [Fig. 1(a)]. To efficiently stop the flow before the onset of sound, the inlet and outlet were short-circuited with the aid of a motorized four-port, two-way diagonal valve, so that the inlet flow path was at the same time rerouted directly to the syringe.

The procedure for acquiring cell images was as follows:

1. Inject cells, stop the flow, and wait for cells to sediment either to the floor or the ceiling of the channel, depending on the density of the suspending medium.
2. Acquire a z-stack of calibration images of cells resting on the floor or ceiling.

3. Inject cells, stop the flow, start image acquisition, and activate the sound at a fixed z-position.
4. Acquire images at 10 fps for a sufficient amount of time. Acquisition time varies from 10 to 30 s for different suspending media.

Top view (y-x) images before and after acoustic migration for three different contrast factors are shown in Fig. 1(c). Each image is constructed with the first acquired frame (initial location of K562 cells in step 4, in white) and the last acquired frame (final location of K562 cells in step 4, highlighted in different colors). The focal plane was set to the mid-height of the channel and the cylindrical lens was removed from the optical path. Cells of positive contrast (blue) move towards the center, while negative contrast cells (red) end up at the walls. For the case of near-zero contrast, the cells neither assemble in the center nor at the walls but instead follow the fluid's velocity field and spread everywhere in the channel.

D. General defocusing particle tracking

The motion of cells was analyzed by the GDPT technique [45,46] which is designed to provide 3D trajectories of particles by using the defocused microscope images of particles. A calibration stack of cell images resting on the channel floor or ceiling (in the case of buoyant cells) was recorded to acquire a lookup table for defocused cell shapes at different relative z-positions. For this purpose, the motorized z stage (MFD, Märzhäuser, Wetzlar GmbH & Co. KG, Wetzlar, Germany) equipped with the microscope was moved along the z-coordinate in steps of 2 μm. During experiments the z-position of the stage was fixed, and the motion of the cells was recorded with an exposure time of 20 ms and at a frame rate of 10 fps.

The acquired images were analyzed in the MATLAB routine GDPTlab [48], which performs a normalized cross-correlation (MATLAB built-in function: normxcorr2) between each particle image in the experiment image set and the images from the calibration stack. To achieve a refinement beyond the reference stack z-levels, the routine finds the calibration image that has the highest correlation value (C_m) and then fits a parabola to the nearest C_m values in the stack to identify the z-level that maximizes the C_m value for the particle. In addition, the code tracks the motion of particles in the x-y plane and finally reconstructs their 3D trajectories.

When imaging inside a liquid-filled microchannel using a dry objective, the differences in refractive index on each side of the glass lid leads to a change in the incidence angle of the light that introduces a measurement error. To compensate for this, separate calibration stacks were recorded for each suspending medium and the measured

z-positions were rescaled by the ratio of the refractive indices of the suspending medium and air, respectively [46].

III. RESULTS

A. Measuring the 3D trajectories of cells by general defocusing particle tracking

First, we set out to establish if GDPT can be employed to track the 3D motion of suspension cells. A basic assumption when tracking particles' z-coordinates by their defocused image is that they are spherical and uniform in size [45]. Since suspension cells are neither perfectly spherical, nor uniform in size, we assessed the accuracy and applicability of the GDPT method in this context. Calibration images were obtained by imaging the cells at rest, on either the microchannel floor or the ceiling, for a range of known z-positions (2 µm intervals) using a motorized microscope stage, [Fig. 2(a)]. Figures 2(b)–2(e) show representative images of fluorescent PS beads and neutrophils, respectively, at four different z-positions. Figures 2(f) and 2(g) show the measured coordinates z_{meas} and the corresponding correlation values C_m obtained by the GDPT code as a function of the known z-coordinate for PS particles (4.9 ± 0.9 µm in diameter) and

neutrophils of diameter 8.3 ± 0.9 µm (Supplemental Material, Fig. S2 [47]), respectively.

For each set of calibration images, containing around 20 or more particles or cells, one particle or cell was selected as a calibration object to be matched with all the other particles or cells in the calibration images. We assessed the spatial resolution of the GDPT technique for tracked z-stacks of cells by investigating the measured z-values in each case for all the known z-positions in terms of standard deviation. The standard deviation plot of z_{meas} (Supplemental Material, Fig. S3 [47]) for PS particles is mostly flat and below 3 µm, and it increases to 5 µm for the last two or three calibration images. The data show the same trend for the cells, growing towards 10 µm for the Jurkat cells.

The normalized error (ε_z) for each case was calculated by the sample standard deviation of $z_{meas} - z$, normalized to the total depth of the channel $H = 150$ µm. The corresponding error, averaged along z, for the PS particles was $\overline{\varepsilon_z} = 0.013$. The same approach was conducted for neutrophils, K562, and Jurkat cells to compare with PS particles. The average error for cells was then measured for neutrophils ($\overline{\varepsilon_z} = 0.016$), K562 cells ($\overline{\varepsilon_z} = 0.017$) and Jurkat cells ($\overline{\varepsilon_z} = 0.025$). All image correlation values C_m were greater than 0.90 (Supplemental Material, Fig. S3 [47]).
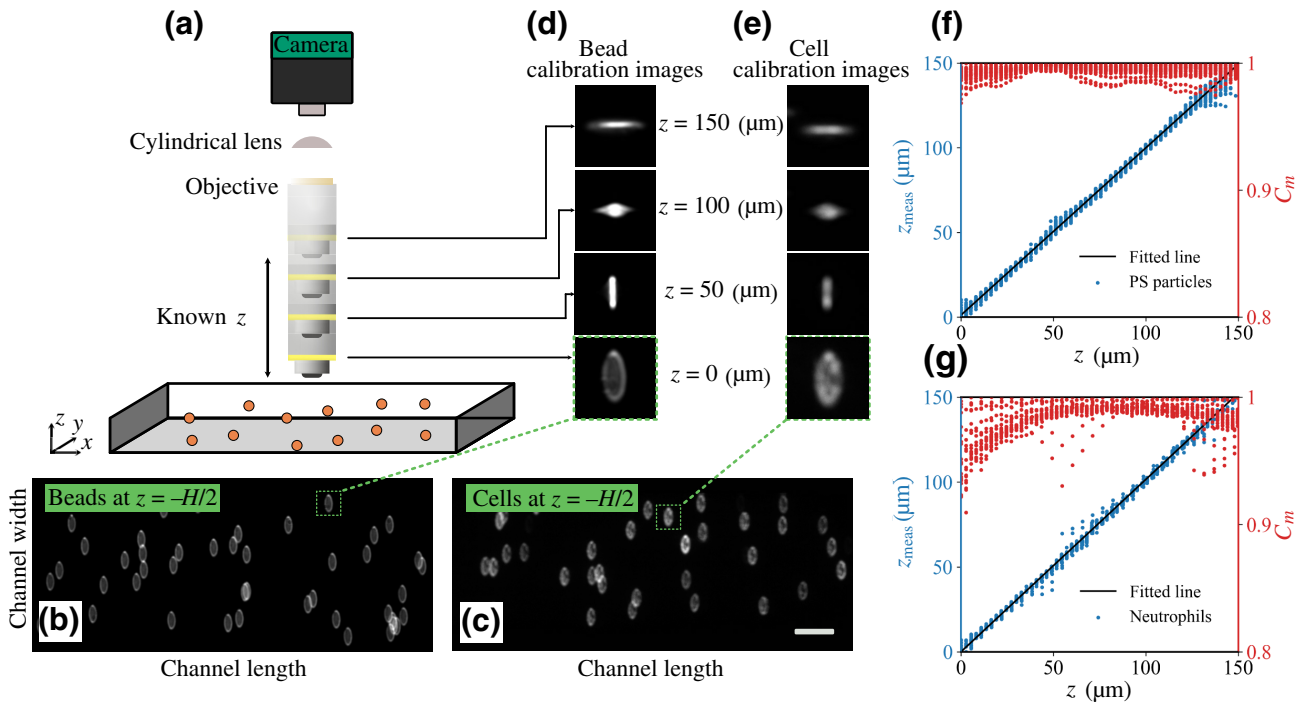

FIG. 2. Measuring cells' z-coordinate. (a) A schematic of the GDPT setup with a cylindrical lens inserted in front of the camera. A representative example of (b) PS beads and (c) neutrophils resting on the channel floor after inserting the cylindrical lens (scale bar 100 µm). Images are taken from above (y-x). Calibration images of (d) beads and (e) neutrophils imaged through the cylindrical lens at different z-coordinates relative to the optical focus. Plots of z_{meas} (blue dots) and correlation coefficient C_m (red dots) versus the microscope-stage z-coordinate for (f) beads (100 beads from three repeats) and (g) neutrophils (100 cells from five repeats).

(a)

Sedimentation trajectories

(b)

PS bead sedimentation velocity
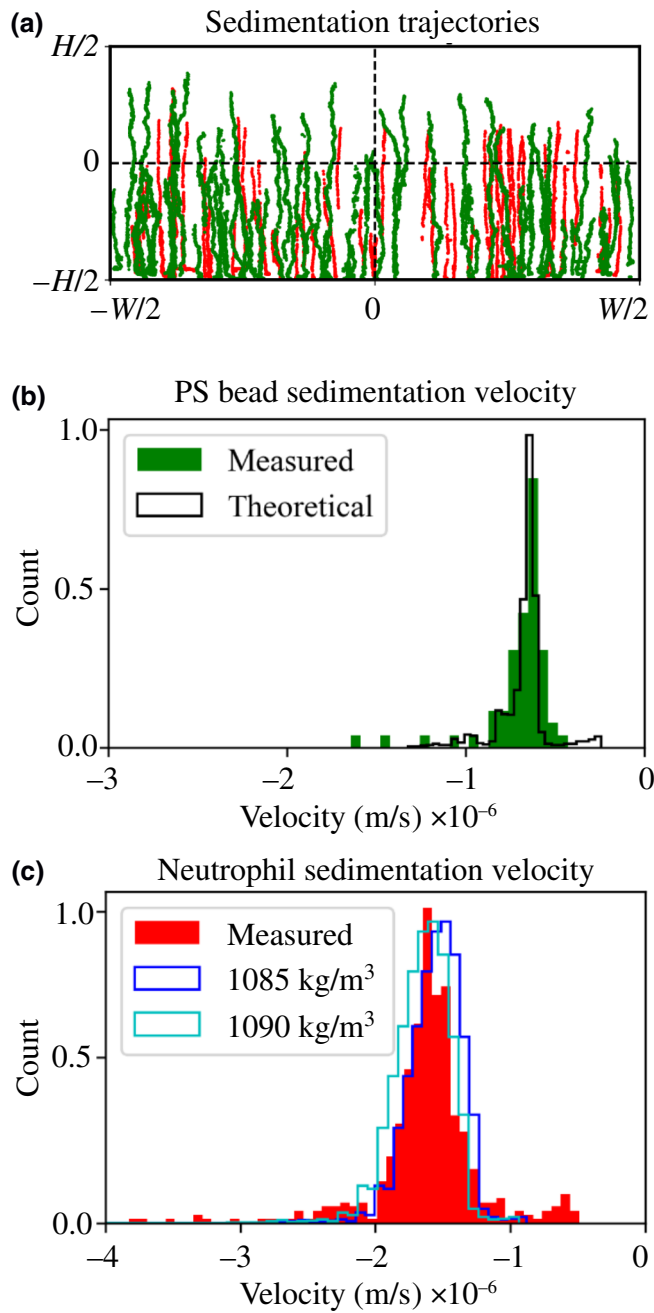
(c)

Neutrophil sedimentation velocity

FIG. 3. Sedimentation of neutrophils and PS particles. (a) Shows the 3D trajectories of sedimenting PS particles (green) and neutrophils (red) in PBS. Plots of the theoretical and measured sedimentation velocity of (b) PS particles and (c) neutrophils. The corresponding size distribution for theoretical velocity calculation was obtained by Coulter counter. The theoretical velocity was calculated for particles having a density of 1049 kg/m^3 and for neutrophils based on an assumption of a uniform cell density of 1085 and 1090 kg/m^3. The number of analyzed tracks ($N = 150$) was normalized.

To analyze how the selection of the reference cell impacts the calibration graph and the corresponding errors, we assigned cells of different relative sizes as a reference

in the calibration. Before inserting the cylindrical lens, an image of the cells was acquired for each calibration stack. We used thresholding to convert the image into a binary version, and then the segmented foreground was analyzed to extract the relative size distribution [49]. Based on the corresponding size table, the smallest, largest, and one medium-sized cell were selected and cross-correlated with the rest of the cells. Our analysis for K562 cells (Supplemental Material, Fig. S4 [47]) and Jurkat cells (Supplemental Material, Fig. S5 [47]) shows that choosing either small or large cells increases the error compared to the medium-sized cell, which has the lowest error. The plots' fitted lines indicate that small cells tend to underestimate, and large cells slightly overestimate, the measured z. For both cell types a maximum offset error e occurs when a small cell is selected as the reference object and when measuring a position close to the ceiling $e_{K562} = -5.74$ µm (PI$_{95}$: ±4.63 µm) for K562 and -5.43 µm (PI$_{95}$: ±7.33 µm) for Jurkat cells. Our investigation of the cross-correlation to the reference library of the out-of-focus cell images confirms that we can obtain an accuracy in determining z within approximately one cell diameter.

B. Measuring cell sedimentation

To demonstrate that we can track cells' z-locations over time, we tracked the trajectories of neutrophils and 4.9-µm-diameter PS particles suspended in PBS while sedimenting by gravitation. Figure 3(a) shows the positions of neutrophils (red dots) and PS particles (green dots) projected onto the y-z plane. We analyzed the velocity data for particles and cells with trajectories longer than 20 µm within $|z| < H/4$ to avoid wall effects.

For each track, the mean and the standard deviation of the velocity were computed, and tracks of a standard deviation greater than 20 µm/s were considered too noisy and therefore excluded. To avoid the overlap between cells' defocused images that can, in principle, introduce new cell tracks, cell samples in high concentration were diluted.

Histograms of the theoretical and experimentally measured sedimentation velocities for the PS particles and the neutrophils are plotted in Figs. 3(b) and 3(c). The theoretical estimates are based on the measured size distributions of particles and neutrophils, respectively, and we derived the sedimentation velocity distributions using Stokes' law under the assumption of $\rho_{PS} = 1049$ kg/m^3 and $\rho_{neutrophils} = 1085$ and 1090 kg/m^3 [50,51]. Particle sedimentation velocities are in good agreement without any fitting and the distribution of the measured sedimentation velocity for neutrophils is close to the theoretical prediction, but they sediment slightly slower than the expected velocity distribution based on $\rho_{neutrophils} = 1090$ kg/m^3. Adjusting the density of neutrophils to 1085 kg/m^3 shifts the theoretical velocity distribution to the right and provides a slightly better match.

C. Cells' migration in a sound field in different suspending media

We then investigated the 3D migration of the cells in an acoustic half-wave microfluidic resonator when suspended in media of increasing acoustic impedance $(Z_f = \rho_f c_f = \sqrt{\rho_f / \kappa_f})$, where ρ_f, c_f and κ_f denotes density, speed of sound and compressibility of the fluid, respectively. To achieve this, cells were suspended in iodixanol solutions of concentrations ranging from 10% to 34%. As described in Sec. II C, the cells were introduced into the channel, and the flow was stopped before the image acquisition was initiated. The sound field was

activated shortly after the image acquisition was started (Fig. 1).

Figure 4 shows overlays of the locations for neutrophil migration in homogeneous media measured in three dimensions for five different iodixanol concentrations (C_{ix}). The trajectories are projected along the channel (x) onto the radial cross section $(y$-z plane). For a low-acoustic-impedance medium $(C_{ix} \leq 22\%,$ $Z_f < 1.67$ MPa s/m) [Figs. 4(a)–4(c)], neutrophils have a positive contrast factor $(\Phi > 0)$, and $\boldsymbol{F}_{\mathrm{rad}}$ moves them towards the pressure node within the five seconds after turning on the sound. As C_{ix} increases, the neutrophils
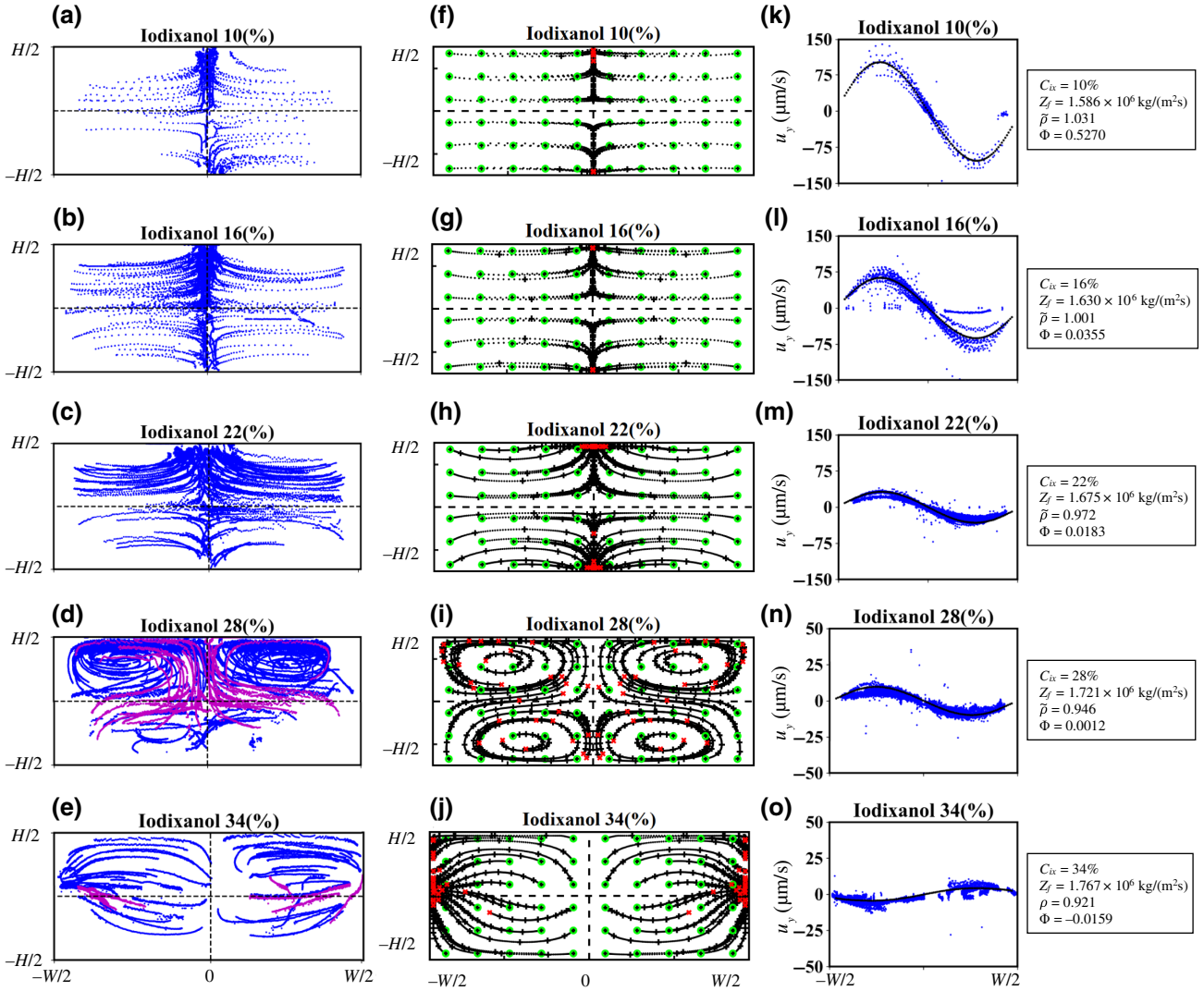

FIG. 4. Three-dimensional trajectories of neutrophils in different concentrations of iodixanol projected along x. (a)–(c) The contrast factor is positive for neutrophils, and they end up in the center of the channel within 10 s of recording after the onset of the sound. (d) In the scenario where the acoustic impedance of the medium matches that of the neutrophils, the acoustic radiation force vanishes. Recording time was 30 s. (e) Trajectories of neutrophils of negative contrast factor forcing them towards the walls. Recording time was 20 s. (a)–(e) Cells that transition from the lower to the upper half are indicated in magenta. (f)–(j) Simulated trajectories of neutrophils for the same range of iodixanol concentrations as in (a)–(e). The initial and final locations of neutrophils in the simulations are marked with green circles and red crosses, respectively. (k)–(o) Experimental (blue dots) and simulated (black dots) data for y-component of neutrophil velocity at mid-height. The time step is 0.1 s for all measured and simulated trajectories. $\tilde{\rho} = \rho_{\mathrm{neutrophils}} / \rho_f$.

move more slowly (observed by the shorter gaps between the dots) due to a lower acoustic contrast when Z_f increases and due to an increased viscosity (η). The trajectories become curved due to the increasing impact of acoustic streaming relative to acoustic radiation. No buoyancy effect can be observed for $C_{ix} \leq 22\%$ on the time scale of the experiment, which is expected since the literature value for neutrophil density, 1090 kg/m^3, is close to that of the medium.

For intermediate acoustic impedance ($C_{ix} = 28\%$, $Z_f = 1.72$ MPa s/m) the acoustic contrast approaches zero [Fig. 4(d)]. Acoustically transparent neutrophils ($\Phi = 0.001$) do not experience radiation forces and therefore follow the acoustic streaming rolls. The trajectories for some of the cells (magenta) in this medium reveal that they are buoyant since they migrate from the lower to the upper half of the resonator.

For higher impedance ($C_{ix} = 34\%$, $Z_f = 1.76$ MPa s/m), the neutrophil migration is indicative of negative acoustic contrast ($\Phi < 0$), and they migrate towards the walls [Fig. 4(e)]. The cell buoyancy causes the cells to congregate at two elevated sites on the sidewalls, and the overall cell migration indicates contributions from radiation, gravity, and streaming.

The simulated trajectories (Appendix A) shown in Figs. 4(f)–4(j) are in good agreement with the corresponding experimental trajectories shown in Figs. 4(a)–4(e) when we assume $E_{ac} = 25.8$ J/m^3 (measured, Appendix B), $2a = 8.30$ μm (measured population average), $\rho_p = 1090$ kg/m^3 (from the literature), and $\kappa_p = 3.663 \times 10^{-10}$ Pa^{-1} (manually fitted). Fitting of the cell compressibility was done manually by comparing experiments and simulations across the investigated range of media until a perceived best match was achieved. The derived cell compressibility was then used to compute the acoustic contrast (Φ). Simulated and experimental data for the y-component of the cell velocity u_y at mid-height are in good agreement [Figs. 4(k)–4(o)].

We also carried out trajectory measurements for Jurkat and K562 cells in the same range of iodixanol concentrations (10% to 34%, in steps of 3%). The 3D trajectories show that the transition from positive to negative contrast happens near $C_{ix} = 19\%$ ($Z_f = 1.65$ MPa s/m) for both cell types (Supplemental Material, Figs. S7 and S8 [47]). The buoyancy effect is more dramatic for these two cell types than for neutrophils since they are larger and have lower density [52]. The trajectories of acoustically transparent K562 cells (14.3 ± 4.0 μm) reveals that they do not even form a proper streaming roll in the upper half of the channel due to their high buoyancy, and they soon find their way towards the ceiling. On the other hand, Jurkat cells (11.4 ± 2.5 μm) still experience streaming contribution due to their smaller size. Generally, at near-zero acoustic contrast, the cell motion patterns are highly sensitive to small differences in the cell size, density, and compressibility.

The considerable variation in motion paths observed for K562 and Jurkat cells can be explained by their greater degree of heterogeneity in terms of their size distributions compared to neutrophils, and possibly also in terms of their density and compressibility, although these two parameters are not investigated in the current study.

D. Classification of 3D trajectories for three different cell types

When separating or categorizing cells of different type using acoustic fields, it is of interest to identify a medium that leads to a desired outcome and to understand how much the populations overlap in terms of their response to sound. While the overall patterns of the 3D trajectories of cells are well described by the numerical model (Fig. 4), there is considerable spread in the trajectories of individual cells, in particular for cells with near-zero acoustic contrast. In an attempt to quantify the overlap, the 3D trajectories of thousands of single cells were analyzed and classified using a neural network approach.

To compare the acoustic migration for the three cell types in a range of media, we constructed a neural network model to classify trajectories as positive, zero, or negative contrast based on manual labeling of 833 Jurkat cell trajectories in different media (Appendix C). Figure 5(a) shows that for $C_{ix} \leq 13\%$, all Jurkat cells have positive contrast, and in the intermediate zone of iodixanol concentrations ($C_{ix} = 16\%$–25%), cells are of all three classes. The percentage of positive-sign trajectories decreases, and negative-sign trajectories grow with increasing C_{ix}, whereas the number of zero-contrast trajectories has a maximum for $C_{ix} = 19\%$. The plot shows that the transition from positive to negative contrast for Jurkat cells seems to be at around 19% iodixanol concentration. For $C_{ix} > 25\%$, Jurkat cells have mostly negative contrast. Figures 5(b) and 5(c) show the neural network predictions for K562 cells and neutrophils, respectively. There is a similar trend between K562 and Jurkat cells. The transition from positive to negative contrast for K562 cells is around 19% iodixanol, for which 84% of the cells have zero contrast. Finally, the classifier predicts neutrophils to change the sign of the acoustic contrast at ($C_{ix} = 28\%$, $Z_f = 1.72$ MPa s/m), which is higher than for both K562 and Jurkat cells.

IV. DISCUSSION

This study shows the 3D measurement of acoustophoretic migration for neutrophils, K562, and Jurkat cells suspended in solutions containing different amounts of iodixanol, leading to an acoustic contrast factor change, from positive, through zero, to negative. To track cells in various media, we successfully extended the application of GDPT to suspension cells.
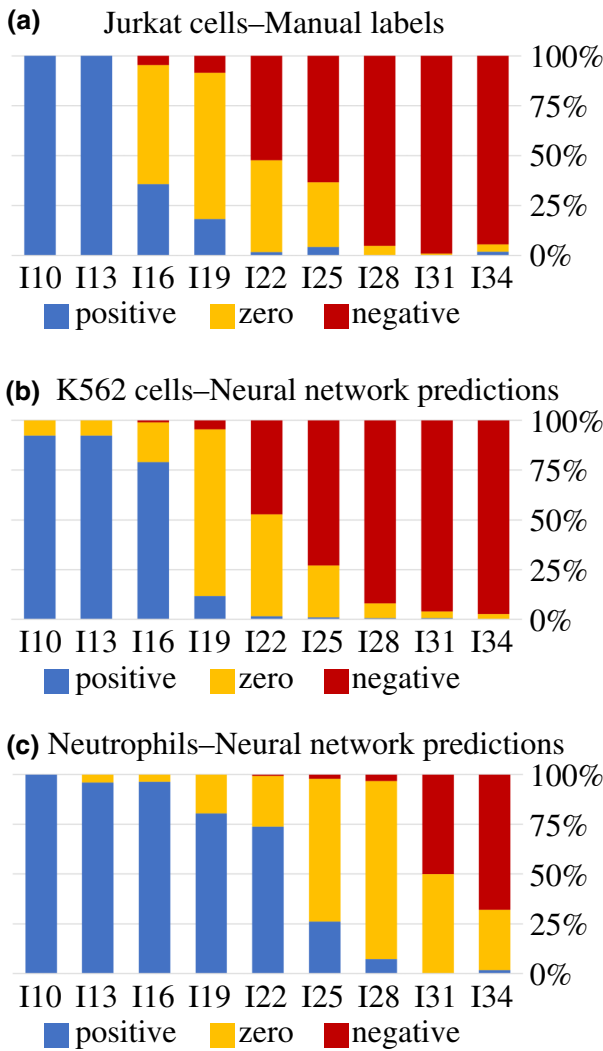
(a) Jurkat cells–Manual labels

(b) K562 cells–Neural network predictions

(c) Neutrophils–Neural network predictions

FIG. 5. Neural network predictions of the sign of the cells' acoustic contrast in different iodixanol concentrations. The model was first trained with Jurkat cell data and then applied to K562 cells and neutrophils.

The sedimentation data for PS particles and neutrophils, shown in Fig. 3, validates our measurement of the z-component of 3D trajectories. The measured sedimentation velocity for neutrophils indicates a good match with a calculated velocity based on uniform cell densities of 1085 and 1090 kg/m^3, respectively. It should be noted that even though density fractionation is common for blood cells, there is a lack of systematic detailed studies of the density of neutrophils. Also, the size and density distributions of neutrophils may differ from one donor to another and depend on the choice of isolation protocol and medium. Neutrophils are sensitive to mechanical and chemical stimuli which can cause activation, and therefore we did not use a neutrophil enrichment protocol based on red blood cell chemical lysis to avoid neutrophils undergoing any phenotypic change since it has been previously shown that

the physical properties of white blood cells alter when exposed to the red blood cell-lysing agents [40]. Still, the sedimentation velocity shows a small peak in the lower range of the sedimentation velocity histogram. We believe it can be related to activated neutrophils or so-called low-density neutrophils since activation of neutrophils has been reported to cause a density reduction [50,51].

The 3D trajectories of neutrophil migration in a sound field in different iodixanol concentrations match well with the simulated trajectories, and this is mainly because neutrophils have a narrow distribution in size and density. Studies by magnetic levitation of cells support that white blood cells do not have as wide a distribution of density as cancer cells do [15,53]. For $C_{ix} = 28\%$, where most of the neutrophils follow the streaming rolls, the effective acoustic impedance is 1.72 MPa s/m, which is somewhat lower than what Augustsson *et al.* [40] reported (approximately 1.74 MPa s/m). The difference may be attributed to small deviations in the cell preparation or to the temperature being different in the experiments since the temperature was not reported or controlled in that study. Although the measured 3D motion of Jurkat and K562 cells (shown in Supplemental Material, Figs. S7 and S8 [47]) generally agrees with the simulations, it is apparent from the trajectories that these cells have less uniform properties in terms of acoustic contrast or size. This heterogeneity is most pronounced for the concentrations where the transition from positive to negative contrast occurs [Supplemental Material, Figs. S7(c) and S8(b) [47]]. Looking at the trajectories, a handful of patterns are present at each C_{ix}, and no single set of simulation parameters can predict the experimental trajectories data. The experimental and simulated trajectory data for $C_{ix} = 25\%$, for Jurkat cells [Supplemental Material, Fig. S7(c) [47]], suggest that their s-shaped migration is governed by streaming and buoyancy, while the measured trajectories also include some tracks having clearly negative contrast, in the same medium [Supplemental Material, Fig. S7(c) [47]]. On the other hand, K562 cells in $C_{ix} = 25\%$ migrate mainly towards the walls, indicative of a lower density or higher compressibility than Jurkat cells [Supplemental Material, Fig. S8(c) [47]].

We observed Jurkat cells to be of zero contrast in the range from $C_{ix} = 19\%$ to 25%, corresponding to a compressibility in the range from 3.71×10^{-10} to 3.92×10^{-10} Pa^{-1}. Riaud *et al.* [38] developed a tilted-angle standing surface acoustic wave acoustophoresis device coupled with resistive pulse sensing to measure the compressibility of Jurkat cells. For an assumed density of 1075 kg/m^3 and a diameter of 11.5 μm, they measured a compressibility of 3.28×10^{-10} Pa^{-1} for Jurkat cells. For the herein reported model those cell parameters would lead to zero acoustic contrast at $C_{ix} \sim 40\%$, which is far above the 19% to 25% that we observed in our experiments.

Olofsson *et al.* [42] measured the ratio of fixed and viable K562 cells in the pressure node, antinode, and

intermediate areas along a straight channel after acoustic actuation for iodixanol concentrations ranging from 0 to 30% w/v and classified cells as having negative, zero, or positive contrast based on their location after a fixed time of sound exposure. From these measurements, living K562 cells were reported to have $Z_{K562} = 1.68 \pm 0.014$ MPa s/m, which is in good agreement with the result presented here that zero contrast for K562 cells falls between $C_{ix} = 19\%$ (1.65 MPa s/m) and $C_{ix} = 22\%$ (1.67 MPa s/m). A drawback with this approach is that a considerable number of cells that are of zero contrast will be falsely classified as either positive or negative based on the region they happen to pass through at the final frame of the recording. Further, the approach of measuring cell properties near zero contrast while ignoring acoustic streaming and buoyancy may, in some scenarios, lead to misinterpretations. To highlight this, Supplemental Material, Fig. S10 [47] shows simulated trajectories for K562 cells for $C_{ix} = 19\%$, 20%, and 21% iodixanol. In C_{ix} 20%, these cells have a slight positive contrast, but the buoyancy effect pulls the cells to the ceiling, and there they will be subject to an acoustic streaming flow that pushes them outwards towards the walls. This results in cells that are of zero or slightly positive contrast ending up in the top corners and will thus be wrongly interpreted as being of negative contrast.

Some caution is called for when interpreting the outcome of the neural network classification scheme. The annotation by experts is by definition subjective and in the scenario of annotating positive, zero or negative contrast, there is no strict definition of the categories. Second, the neural network approach is challenging to generalize beyond the cell type used in the training set because the neural network does not provide information about the underlying physical mechanisms. Nevertheless, the results highlight the heterogeneity at single-cell level which has implications for the ability to separate or categorize cells by acoustic fields in homogeneous media. Figure 5 shows that even if there is a clear difference between neutrophils and the other two cell types, the transition from positive to negative contrast is not distinct for any of the cell types examined which would lead to a considerable contamination in a separation setting or a misclassification if used for classification of cells. Separation approaches such as time-of-flight separation across a cell-free media region, or isoacoustic focusing, may therefore offer better performance both to classify and separate cells based on their type. The major reason for this is that acoustic streaming does not affect the outcome to a high degree in those settings.

Looking ahead, since the cell trajectories indeed carry information related to cell size, density, and compressibility, alternative ways of analyzing these cell trajectories can be explored that can be informative on optimized separation strategies or cell categorization. One approach could be to fit the trajectories of single cells to the numerical model using the underlying cell properties as fitting parameters. What makes this approach challenging is that many combinations of a_{cell}, ρ_{cell}, and κ_{cell} can lead to very similar trajectories, which leads to uncertain determination when fitting these parameters. This puts great demand on the model to match the real system and the accuracy of the 3D tracking. The current model ignores near-wall effects on the cells, cells are assumed to be spherical and have homogenous properties, and the pressure field is assumed to be perfectly 1D and symmetric around $y = 0$. This paper shows that acoustic cell focusing is clearly a 3D phenomenon even in its most basic configuration, and we envision that 3D tracking of single cells will be an important tool in the further exploration of acoustofluidic cell handling systems and the underlying physics.

V. CONCLUSIONS

We have measured the 3D trajectories of living suspension cells undergoing acoustic focusing using a standard epifluorescence microscope. Our main conclusion is that for cells with near-zero acoustic contrast, buoyancy and streaming effects are not negligible. To further optimize acoustic cell separations, accurate knowledge about the size, density, and compressibility at the single-cell level will become important. After reviewing the literature, we can conclude that there is currently no accepted standard to measure the acoustic properties of cells. We propose that future work should be directed towards the establishment of a well-validated method for simultaneous measurement of density, compressibility, and size at the single-cell level. In that quest, we believe that 3D tracking of cells may turn out to be a very useful tool.

APPENDIX A: SIMULATED PARTICLE TRAJECTORIES

Synthetic cell trajectories were generated according to a previously described method where spherical particles are propelled by gravity, acoustic streaming, and acoustic radiation in a homogenous medium in a half-wavelength 1D resonance [32]. We assumed that (i) cells are spherical and have homogeneous density and compressibility,

(ii) gravity acts in the negative z-direction, (iii) the acoustic radiation force on particles can be accurately modeled by the classical Gor'kov theory [54] with a thermoviscous correction [55], and (iv) the acoustic streaming field along the channel bottom and ceiling is well approximated by Rayleigh's analytical solution [31]. We ignored wall effects on the Stokes drag force acting on the cells.

The acoustic streaming field was solved by finite-element modeling in COMSOL Multiphysics (creeping flow) by applying a moving wall boundary condition $u_y = 3E_{ac}/(2c_f \rho_f)\sin(2k_y y)$, where k_y is the wavevector. Values for c_f, ρ_f, and viscosity of iodixanol solutions at different concentrations were taken from Refs. [40,52]. The velocity field was imported in MATLAB, where trajectories were obtained through the fourth-order Runge-Kutta method as implemented in the function ode45.

APPENDIX B: DETERMINATION OF THE ACOUSTIC ENERGY DENSITY

To determine the acoustic energy density, 3D trajectories of hundreds of 1.1-μm-diameter PS particles of known density and compressibility were recorded using the GDPT method. Tracks or parts of tracks in the range $|z| < H/8$ and $|y| < W/4$ were analyzed, and their velocities were fitted to a function $u_y = u_0 \sin(2k_y y + \alpha)$ where $k_y = 2\pi/\lambda$ and u_0 and α are free fitting parameters. At mid-height, away from the sidewalls, both acoustic radiation and acoustic streaming follow a sinusoidal dependency on y and are well approximated by the classical analytical parallel-plate model for acoustic streaming [31,56]. Thus, the acoustic energy density can be derived through $E_{ac} = u_0/(f_a + f_b)$, where $f_a = 2\Phi k_y a^2/3\eta$ accounts for the acoustic radiation velocity, and $f_b = 3a^2/4\rho_f c_f$, accounts for the acoustic streaming.

The approach to determining the acoustic energy density relies on knowing the PS beads' size, density, and compressibility. However, for particles below the critical particle diameter (approximately 2 μm) [32,33,56], the acoustic streaming will dominate the motion, which puts less demand on the accuracy of determining the density and compressibility of the particles. We nevertheless measured the density and compressibility for the same type of particles (4.9 μm in diameter) to be 1049 kg/m³ and 2.73×10^{-10} Pa^{-1}, respectively, following the method presented in Ref. [34]. The size of the particles was measured using the Coulter principle (Multisizer 3, Beckman Coulter).

To ensure a narrow distribution in density, we did repeated steps of centrifugation (Eppendorf Centrifuge 5427 R) to fraction the stock solution of the beads based on their density. The centrifuge was equipped with an air-cooling function to keep the temperature constant. We first prepared the stock solution of water by adding 0.1% Tween

20. We used the stock solution to make working solutions of different densities by adding iodixanol. Working solutions had densities ranging from 1045 to 1050 kg/m³ in steps of 1 kg/m³. We measured the density for each solution by using a density and sound velocity meter (DSA 5000 M, Anton Paar GmbH, Graz, Austria). To purify the beads in each batch, we transferred 500 μL of the bead solution to a tube, and the particles were spun down. We discarded the supernatant and resuspended the pellet in a denser solution starting from 1045 kg/m³. We repeated the steps until we got no pellet at the bottom of the tube. The most abundant fraction of neutrally buoyant particles was found at a density of 1049 kg/m³. We collected a sufficient number of particles by repeating the procedure for several fractions of beads.

The isolated particles in their neutral buoyancy medium were then analyzed in the density and sound velocity meter following the procedure of Cushing *et al.* [34] to measure their compressibility. In brief, the measurement is based on measuring the speed of sound of the suspension and the particle-free medium. Suspension of microparticles with a volume fraction of f_v causes the change in the fluid speed of sound from c_f to c_s. The relative speed of sound $\tilde{c} = c_s/c_f$ given by Wood's equation reduces to a linear function $\beta(\tilde{\rho}, \tilde{\kappa})f_v + 1$ if $f_v \ll 1$. $\tilde{\rho}$ and $\tilde{\kappa}$ are the relative density and compressibility of the microparticles, respectively. At neutral buoyancy, the microparticle and the fluid densities are identical, so $\tilde{\rho} = 1$, and the slope β will only be a function of the relative compressibility ($\tilde{\kappa} = \kappa_p/\kappa_f$). We measured the relative speed of sound for a range of volume fractions, calculated $\beta(\tilde{\kappa}, 1)$ and extracted κ_p from β and κ_f (Supplemental Material, Fig. S6 [47]). The volume fraction of microparticles suspension [2%, 1%, and 0.5% (%vol)] was obtained by electrical resistance sizing in a Coulter Counter (Multisizer 3, Beckman Coulter).

APPENDIX C: CLASSIFICATION SCHEME FOR 3D TRAJECTORIES

We classified the 3D trajectories of cells based on their acoustic contrast. To determine the acoustic contrast, we used a neural network approach. For each cell experiment containing Jurkat cells, K562 cells, and neutrophils, the corresponding particle trajectories for 1 μm PS were obtained to quantify the acoustic energy density through the acoustic streaming flow. The 1-μm particle locations were also used to establish the GDPT coordinates of the channel perimeter, as these particles are abundant and are assumed to spread in the whole channel. The data were then shifted and scaled to represent the channel. The trajectories were smoothed by robust locally weighted scatterplot smoothing (rlowess) with a window size of 6 elements, and if they contained large gaps greater than 12.5 μm, they were split into two separate tracks. Tracks were discarded if they were shorter than 49 points or if

they migrated less than 9% of the channel width in the horizontal direction since they were deemed not to show enough information to determine the underlying particle properties.

Images were generated to implement a neural network representing the GDPT particle and cell trajectories in the y-z plane. Each track was then plotted in a 224×224 pixel RGB image. Each data point in the GDPT trajectory was plotted as one pixel by rounding off the position to the nearest pixel position. The pixels' color was determined in a saturable color gradient representing velocity, ranging from blue (slow) to yellow (fast). The start and endpoints were marked with green and red dots, respectively (Supplemental Material, Fig. S9 [47]). Image sets were created for each cell type for iodixanol concentrations ranging from 10% to 34%.

A dataset of images of Jurkat cell trajectories was annotated by four experts as having positive, negative, zero, or undeterminable acoustic contrast, considering the effect of acoustic streaming and acoustic radiation. The images were gathered from iodixanol concentrations of 10% to 34% including examples of all three acoustic contrast classes. These Jurkat image-label pairs were then used to train neural networks in TensorFlow [57]. The Jurkat images, 833 in total, were split into a training set, 80%, and a test set, 20%, by random sampling. The neural network was trained until the accuracy on the test set reached 98.8%. With the model classifying 165 out of 167 Jurkat trajectories correctly, the confidence of the model was assumed to be high. The model trained on the Jurkat dataset was then applied on the unlabeled K562 and neutrophil datasets to predict the acoustic contrast.

The neural network model consisted of three convolution layers with subsequent max pooling with a 128-node fully connected layer on top before the final prediction layer. The classes used were positive, zero, and negative acoustic contrast. Horizontal and vertical random flip data augmentation was used in training. The neural network was then employed to classify all valid tracks for each iodixanol concentration to determine the corresponding sign for the acoustic contrast.

---

[1] J. Sibbitts, K. A. Sellens, S. Jia, S. A. Klasner, and C. T. Culbertson, Cellular analysis using microfluidics, Anal. Chem. **90**, 65 (2018).

[2] S. Battat, D. A. Weitz, and G. M. Whitesides, An outlook on microfluidics: The promise and the challenge, Lab Chip **22**, 530 (2022).

[3] C. W. Fung, S. N. Chan, and A. R. Wu, Microfluidic single-cell analysis—toward integration and total on-chip analysis, Biomicrofluidics **14**, 021502 (2020).

[4] K. C. M. Lee, J. Guck, K. Goda, and K. K. Tsia, Toward deep biophysical cytometry: Prospects and challenges, Trends Biotechnol. **39**, 1249 (2021).

[5] J. A. Davis, D. W. Inglis, K. J. Morton, D. A. Lawrence, L. R. Huang, S. Y. Chou, J. C. Sturm, and R. H. Austin, Deterministic hydrodynamics: Taking blood apart, Proc. Natl. Acad. Sci. U. S. A. **103**, 14779 (2006).

[6] B. R. Mutlu, J. F. Edd, and M. Toner, Oscillatory inertial focusing in infinite microchannels, Proc. Natl. Acad. Sci. U. S. A. **115**, 7682 (2018).

[7] H. Haddadi, H. Naghsh-Nilchi, and D. Di Carlo, Separation of cancer cells using vortical microfluidic flows, Biomicrofluidics **12**, 014112 (2018).

[8] N. Norouzi, H. C. Bhakta, and W. H. Grover, Sorting cells by their density, PLoS One **12**, e0180520 (2017).

[9] W. H. Grover, A. K. Bryan, M. Diez-Silva, S. Suresh, J. M. Higgins, and S. R. Manalis, Measuring single-cell density, Proc. Natl. Acad. Sci. U. S. A. **108**, 10992 (2011).

[10] G. E. Neurohr and A. Amon, Relevance and regulation of cell density, Trends Cell Biol. **30**, 213 (2020).

[11] M. Urbanska, H. E. Munoz, J. S. Bagnall, O. Otto, S. R. Manalis, D. Di Carlo, and J. Guck, A comparison of microfluidic methods for high-throughput cell deformability measurements, Nat. Methods **17**, 587 (2020).

[12] P. Rosendahl, K. Plak, A. Jacobi, M. Kraeter, N. Toepfner, O. Otto, C. Herold, M. Winzi, M. Herbig, Y. Ge, *et al.*, Real-time fluorescence and deformability cytometry, Nat. Methods **15**, 355 (2018).

[13] M. Xavier, S. H. Holm, J. P. Beech, D. Spencer, J. O. Tegenfeldt, R. O. C. Oreffo, and H. Morgan, Label-free enrichment of primary human skeletal progenitor cells using deterministic lateral displacement, Lab Chip **19**, 513 (2019).

[14] E. M. Darling and D. Di Carlo, High-throughput assessment of cellular mechanical properties, Annu. Rev. Biomed. Eng. **17**, 35 (2015).

[15] N. G. Durmus, C. Tekin, S. Guven, K. Sridhar, A. A. Yildiz, G. Calibasi, I. Ghiran, R. W. Davis, L. M. Steinmetz, and U. Demirci, Magnetic levitation of single cells, Proc. Natl. Acad. Sci. U. S. A. **112**, E3661 (2015).

[16] S. C. Ge, Y. Z. Wang, N. J. Deshler, D. J. Preston, and G. M. Whitesides, High-throughput density measurement using magnetic levitation, J. Am. Chem. Soc. **140**, 7510 (2018).

[17] D. Vercruysse, A. Dusa, R. Stahl, G. Vanmeerbeeck, K. de Wijs, C. X. Liu, D. Prodanov, P. Peumans, and L. Lagae, Three-part differential of unlabeled leukocytes with a compact lens-free imaging flow cytometer, Lab Chip **15**, 1123 (2015).

[18] G. Holzner, B. Mateescu, D. Van Leeuwen, G. Cereghetti, R. Dechant, S. Stavrakis, and A. Demello, High-throughput multiparametric imaging flow cytometry: Toward diffraction-limited sub-cellular detection and monitoring of sub-cellular processes, Cell Rep. **34**, 108824 (2021).

[19] M. A. Burguillos, C. Magnusson, M. Nordin, A. Lenshof, P. Augustsson, M. J. Hansson, E. Elmér, H. Lilja, P. Brundin, T. Laurell, *et al.*, Microchannel acoustophoresis does not impact survival or function of microglia, leukocytes or tumor cells, PLoS One **8**, e64233 (2013).

[20] M. Wiklund, Acoustofluidics 12: Biocompatibility and cell viability in microfluidic acoustic resonators, Lab Chip **12**, 2018 (2012).

[21] T. Laurell and A. Lenshof, *Microscale Acoustofluidics* (RSC Publishing, Cambridge, 2015).

[22] P. Zhang, H. Bachman, A. Ozcelik, and T. J. Huang, Acoustic microfluidics, Annu. Rev. Anal. Chem. **13,** 17 (2020).

[23] P. Augustsson, C. Magnusson, M. Nordin, H. Lilja, and T. Laurell, Microfluidic, label-free enrichment of prostate cancer cells in blood based on acoustophoresis, Anal. Chem. **84,** 7954 (2012).

[24] X. Y. Ding, Z. L. Peng, S. C. S. Lin, M. Geri, S. X. Li, P. Li, Y. C. Chen, M. Dao, S. Suresh, and T. J. Huang, Cell separation using tilted-angle standing surface acoustic waves, Proc. Natl. Acad. Sci. U. S. A. **111,** 12992 (2014).

[25] E. U. Anand, C. Magnusson, A. Lenshof, Y. Ceder, H. Lilja, and T. Laurell, Two-step acoustophoresis separation of live tumor cells from whole blood, Anal. Chem. **93,** 17076 (2021).

[26] D. Van Assche, E. Reithuber, W. Qiu, T. Laurell, B. Henriques-Normark, P. Mellroth, P. Ohlsson, and P. Augustsson, Gradient acoustic focusing of sub-micron particles for separation of bacteria from blood lysate, Sci. Rep. **10,** 3670 (2020).

[27] M. Nordin and T. Laurell, Two-hundredfold volume concentration of dilute cell and particle suspensions using chip integrated multistage acoustophoresis, Lab Chip **12,** 4610 (2012).

[28] D. Carugo, T. Octon, W. Messaoudi, A. L. Fisher, M. Carboni, N. R. Harris, M. Hill, and P. Glynne-Jones, A thin-reflector microfluidic resonator for continuous-flow concentration of microorganisms: A new approach to water quality analysis using acoustofluidics, Lab Chip **14,** 3830 (2014).

[29] A. Lenshof, A. Ahmad-Tajudin, K. Jaras, A. M. Sward-Nilsson, L. Aberg, G. Marko-Varga, J. Malm, H. Lilja, and T. Laurell, Acoustic whole blood plasmapheresis chip for prostate specific antigen microarray diagnostics, Anal. Chem. **81,** 6030 (2009).

[30] P. Augustsson and T. Laurell, Acoustofluidics 11: Affinity specific extraction and sample decomplexing using continuous flow acoustophoresis, Lab Chip **12,** 1742 (2012).

[31] L. Rayleigh, On the circulation of air observed in Kundt's tubes, and on some allied acoustical problems, Philos. Trans. R. Soc. London **175,** 1 (1884).

[32] W. Qiu, H. Bruus, and P. Augustsson, Particle-size-dependent acoustophoretic motion and depletion of micro- and nano-particles at long timescales, Phys. Rev. E **102,** 103108 (2020).

[33] P. B. Muller, M. Rossi, ÁG Marín, R. Barnkob, P. Augustsson, T. Laurell, C. J. Kähler, and H. Bruus, Ultrasound-induced acoustophoretic motion of microparticles in three dimensions, Phys. Rev. E **88,** 023006 (2013).

[34] K. W. Cushing, F. Garofalo, C. Magnusson, L. Ekblad, H. Bruus, and T. Laurell, Ultrasound characterization of microbead and cell suspensions by speed of sound measurements of neutrally buoyant samples, Anal. Chem. **89,** 8917 (2017).

[35] P. Augustsson, R. Barnkob, C. Grenvall, T. Deierborg, P. Brundin, H. Bruus, and T. Laurell, *Miniaturized Systems for Chemistry and Life Sciences 2010* (Chemical and Biological Microsystems Society, Groningen, 2010).

[36] H. Wang, Z. Liu, D. M. Shin, Z. G. Chen, Y. Cho, Y.-J. Kim, and A. Han, A continuous-flow acoustofluidic cytometer for single-cell mechanotyping, Lab Chip **19,** 387 (2019).

[37] F. Garofalo, A. Lenshof, A. Urbansky, F. Olm, A. C. Bonestroo, L. Ekblad, S. Scheding, and T. Laurell, Statistic estimation of cell compressibility based on acoustophoretic separation data, Microfluid. Nanofluid. **24,** 64 (2020).

[38] A. Riaud, W. Wang, A. L. P. Thai, and V. Taly, Mechanical Characterization of Cells and Microspheres Sorted by Acoustophoresis with In-Line Resistive Pulse Sensing, Phys. Rev. Appl. **13,** 034058 (2020).

[39] D. Hartono, Y. Liu, P. L. Tan, X. Y. S. Then, L.-Y. L. Yung, and K.-M. Lim, On-chip measurements of cell compressibility via acoustic radiation, Lab Chip **11,** 4072 (2011).

[40] P. Augustsson, J. T. Karlsen, H. W. Su, H. Bruus, and J. Voldman, Iso-acoustic focusing of cells for size-insensitive acousto-mechanical phenotyping, Nat. Commun. **7,** 11556 (2016).

[41] J. M. Dabbi, Y. Shi, A. Mertiri, R. J. Christianson, and J. Fiering, in *2021 21st International Conference on Solid-State Sensors, Actuators and Microsystems (Transducers)* (IEEE, 2021).

[42] K. Olofsson, B. Hammarström, and M. Wiklund, Acoustic separation of living and dead cells using high density medium, Lab Chip **20,** 1981 (2020).

[43] A. Urbansky, P. Ohlsson, A. Lenshof, F. Garofalo, S. Scheding, and T. Laurell, Rapid and effective enrichment of mononuclear cells from blood using acoustophoresis, Sci. Rep. **7,** 17161 (2017).

[44] K. M. Taute, S. Gude, S. J. Tans, and T. S. Shimizu, High-throughput 3D tracking of bacteria on a standard phase contrast microscope, Nat. Commun. **6,** 8776 (2015).

[45] R. Barnkob, C. J. Kähler, and M. Rossi, General defocusing particle tracking, Lab Chip **15,** 3556 (2015).

[46] R. Barnkob and M. Rossi, General defocusing particle tracking: Fundamentals and uncertainty assessment, Exp. Fluids **61,** 110 (2020).

[47] See Supplemental Material at http://link.aps.org/supplemental/10.1103/PhysRevApplied.19.014046 for a further description and photograph of the chip, measured particle sizes, error analyses of measured *z*, measured speed of sound of particles, and supplemental trajectories of cells.

[48] 3d particle tracking using defocusing, https://defocustracking.com/

[49] S. van der Walt, J. L. Schönberger, J. Nunez-Iglesias, F. Boulogne, J. D. Warner, N. Yager, E. Gouillart, T. Yu, and The scikit-image contributors, Scikit-image: Image processing in Python, PeerJ **2,** e453 (2014).

[50] G. R. Hardisty, F. Llanwarne, D. Minns, J. L. Gillan, D. J. Davidson, E. G. Findlay, and R. D. Gray, High purity isolation of low density neutrophils casts doubt on their exceptionality in health and disease, Front. Immunol. **12,** 625922 (2021).

[51] S. O. Pember, K. C. Barnes, S. J. Brandt, and J. M. Kinkade, Density heterogeneity of neutrophilic polymorphonuclear leukocytes - gradient fractionation and relationship to chemotactic stimulation, Blood **61,** 1105 (1983).

[52] A. Zipursky, E. Bow, R. S. Seshadri, and E. J. Brown, Leukocyte density and volume in normal subjects and in

patients with acute lymphoblastic leukemia, Blood **48**, 361 (1976).

[53] K. Delikoyun, S. Yaman, E. Yilmaz, O. Sarigil, M. Anil-Inevi, K. Telli, O. Yalcin-Ozuysal, E. Ozcivici, and H. C. Tekin, Hologlev: A hybrid magnetic levitation platform integrated with lensless holographic microscopy for density-based cell analysis, ACS Sens. **6**, 2191 (2021).

[54] L. P. Gor'kov, On the forces acting on a small particle in an acoustical field in an ideal fluid, Sov. Phys. Dok. **6**, 773 (1962).

[55] M. Settnes and H. Bruus, Forces acting on a small particle in an acoustical field in a viscous fluid, Phys. Rev. E **85**, 016327 (2012).

[56] R. Barnkob, P. Augustsson, T. Laurell, and H. Bruus, Acoustic radiation- and streaming-induced microparticle velocities determined by microparticle image velocimetry in an ultrasound symmetry plane, Phys. Rev. E **86**, 056307 (2012).

[57] An end-to-end open source machine learning platform, https://www.tensorflow.org/

Correction: The Supplemental Material was mistakenly removed during the production process and has been restored. The reference to the Supplemental Material and all citations in text have also been restored. Appendix D was inserted in error and has been removed.